Nuclear Science and Techniques (2026) 37:11
https://doi.org/10.1007/s41365-025-01811-3

# Tender energy spectroscopy beamline at the Shanghai Synchrotron Radiation Facility

Shu-Min Yang[1] · Ling-Ling Guo[1] · Bing Nan[1] · Ying Zhao[1] · Yan-Qing Wu[1] · Zhi Guo[1] · Chen Tian[1] · Bo Zhao[1] · Chao-Fan Xue[1] · Jun Zhao[1] · Shuang Song[1,2] · Zhen-Ye Liang[1,2] · Li-Na Li[1] · Yong Wang[1] · Ren-Zhong Tai[1]

Received: 18 September 2024 / Revised: 20 January 2025 / Accepted: 12 February 2025 / Published online: 7 December 2025


## Abstract

This paper describes the design and performance of the tender energy spectroscopy beamline (BL16U1), a phase II beamline, at the Shanghai Synchrotron Radiation Facility. The beamline, based on an in-vacuum undulator source with 26 mm period, provides an operable energy range between 2.1 keV and 16 keV, covering the K-edges of P to Rb and $L_3$-edges of Zr to Bi. The principal optical elements of the beamline are a toroidal mirror, a liquid nitrogen-cooled double-crystal monochromator, a high-harmonic-rejection mirror, and two pairs of Kirkpatrick–Baez (KB) mirrors. Three end-stations, including non-focusing, microprobe, and sub-microprobe types, are installed on the beamline. X-ray fluorescence (XRF) and X-ray absorption spectroscopy (XAS), including X-ray absorption near-edge structure (XANES) and extended X-ray absorption fine structure (EXAFS), are performed under vacuum or He atmosphere at the non-focusing end-station (with a beam spot size of ~ 670 μm × 710 μm). Using two KB mirrors systems, micro-XRF (μXRF) mapping and micro-XANES (μXANES) studies can be performed with a spot size of approximately ~ 3.3 μm × 1.3 μm at the microprobe end-station and with a smaller spot size of ~ 0.5 μm × 0.25 μm at the sub-microprobe end-station. The non-focusing end-station was officially opened to users in January 2024. The microprobe and sub-microprobe end-stations will be opened to users in the near future. This paper presents the characteristics, short-term technical developments, and early experimental results of this new beamline.

**Keywords** Tender energy X-ray spectroscopy · X-ray fluorescence · SSRF · X-ray absorption spectroscopy (XAS) · Microprobe

## 1 Introduction

As the third-generation synchrotron radiation light source in China, the Shanghai Synchrotron Radiation Facility (SSRF) is equipped with a storage ring energy of 3.5 GeV, circumference of 432 m, and emittance of approximately 3.9 nrad [1]. The SSRF opened to users in 2009 with seven phase-I beamlines [2]. Over the following few years, six additional beamlines were built as part of a Follow-up Beamline Program. Within the framework of the SSRF Phase II Beamline Project (2016) [3, 4], 16 new beamlines and more than 30 end-stations have been built. The photon energy extends to previously uncovered regions such as the tender X-ray region (BL16U1), super-hard X-ray region, and low-energy gamma-ray region.

XAS techniques, including X-ray absorption near-edge structure (XANES) and extended X-ray absorption fine structure (EXAFS), have been recognized as efficient and

This work was supported by the National Key R&D Program of China (No. 2021YFA1601003) and the financial support of the SSRF Phase II project). We also thank the staff in the beam engineering technology department at SSRF for their help with beamline design and installation.

✉ Yan-Qing Wu
wuyanqing@sari.ac.cn

✉ Yong Wang
wangyong@sari.ac.cn

✉ Ren-Zhong Tai
tairz@sari.ac.cn

[1] Shanghai Advanced Research Institute, Chinese Academy of Sciences, Shanghai 201204, China

[2] University of Chinese Academy of Sciences, Beijing 100049, China

comprehensive analytical tools for probing the electronic and local atomic structure order of metals/elements, owing to their advantages in element selectivity, valence state identification, and characterization of local atomic structures. Up to now, XAS platforms, including the soft X-ray spectromicroscopy beamline (BL08U1A, STXM, 250 eV to 2000 eV), the X-ray absorption fine-structure beamline (BL14W1, XAFS, 4.5 keV to 50 keV), the hard X-ray microfocusing beamline (BL15U1, 5 keV to 20 keV [5]), and the hard X-ray spectroscopy beamline (BL11B, 5 keV to 30 keV) et al., can be supported to users from soft X-ray to hard X-ray in SSRF.

Owing to the SSRF Phase II Beamline Project, the tender energy spectroscopy beamline (BL16U1) is the only beamline designed to fulfill the tender photon energy gap in the SSRF. The tender energy range of 2 keV to 5 keV, between the energy ranges of soft and hard X-rays, covers the K-edges of those elements such as phosphorus (P), sulfur (S), chlorine (Cl), potassium (K), calcium (Ca), and titanium (Ti) et al., which are important elements in soil and environmental sciences [6–12], geologic and cosmologic materials [13–15], life sciences [16–18], catalysis, and archeology sciences [19, 20]. The tender energy range of 2 keV to 5 keV also covers the L edges of Mo to I, which are important elements in novel materials [21], mineral resources [22], environmental contaminants, and biological toxins [23]. Several beamlines available worldwide focus on the tender X-ray energy region, including the Diamond-I18 ( 2 keV to 20.7 keV) [24], SLS-PhoenixI ( 0.8 keV to 8 keV) [25], CLS-SXRMB ( 1.7 keV to 10 keV) [26], ESRF-ID21 ( 2 keV to 10 keV) [27], 8-BM at NSLS-II ( 2 keV to 5.5 keV) [28], the BL27SU at SPring8 (2.1 keV to 3.3 keV) [29], the 4B7A at BSRF ( 1.75 keV to 6.0 keV) [30], and the TPS 32A at NSRRC ( 1.7 keV to 11 keV) [31]. XAS and XRF imaging using microprobes are the main research methods used in these beamlines.

Taking advantage of the high brightness of SSRF, the BL16U1 beamline was designed to cover the X-ray energy range of 2.1 keV to 16 keV using an U26 in-vacuum undulator (IVU). In addition to the tender X-ray energy range, the energy range of the BL16U1 beamline covers those of most of the transition metals and non-metallic elements, especially the ones used in the field of energy, catalysis, and related areas (such as titanium, nickel, iron, gold, platinum, and palladium). Based on a toroidal mirror, a liquid nitrogen-cooled double-crystal monochromator, and a high-harmonic-rejection mirror, XAS can be obtained at the non-focusing end-station with a spot size of ~ 670 μm × 710 μm. The samples were operated under vacuum (lower than 1 mbar). However, if the samples are aqueous, helium gas is purged into the vessel, and no vacuum is used. Based on two pairs of KB mirrors, XANES and XRF mapping will be performed at the microprobe end-station with a spot size of approximately ~ 3.3 μm × 1.3 μm and at the sub-microprobe end-station with a smaller spot size of ~ 0.5 μm × 0.25 μm. The BL16U1 beamline construction was finished in Jul. 2023, and the non-focusing end-station has been officially opened to users since January 2024. The microprobe and sub-microprobe end-stations will be opened to users in the near future. The beamline design, short-term technical developments, and early experimental results are described in this paper.

## 2 Beamline

Specific optimizations of beamline design were conducted to meet the flux and focusing requirements of the beamline. An undulator source was used to obtain a high flux density in small spot sizes for microprobe XRF imaging. A high-angular-range monochromator design is required for a low critical energy of 2.1 keV. Harmonic rejection mirrors with different incident angles were used for different energy ranges, and different coatings were used to avoid absorption edges from the mirror coating. According to the properties of the user samples, vacuum or He atmosphere can be opened to the users.

### 2.1 Light source

The upstream of a 12 m long-canted long straight section in the SSRF was selected as the light source for the tender energy spectroscopy beamline, and the downstream section ( 3.06 m long) was used for the fast X-ray imaging beamline (BL16U2) [32]. An U26 IVU with a 3.2 m length, 26 mm period, and 6 mm minimum gap was chosen as the light source. Detailed information regarding the undulator of the BL16U1 beamline is provided in Table 1. The maximum magnetic field strength exceeded 1.02 T, with a total power greater than 7.7 kW. By tuning the gap from 6 mm to 15 mm, 1–7$^{th}$ harmonics and X-ray energy ranges from 2.1 keV to 16 keV can be generated.

**Table 1** Main characteristics of the U26 IVU

| Parameter | Value |
|---|---|
| Period (mm) | 26 |
| Length (m) | 3.2 |
| Number of periods | 123 |
| Maximum magnet field (T) | 1.02 |
| Minimum gap (mm) | 6 |
| Maximum *k* value | 2.48 |
| Fundamental energy (keV) | 1.1−3.3 |
| Maximum power (kW) | 7.7 |

Synchrotron radiation from an undulator source (planar mode) has high brilliance and a narrow spectral range, which is too narrow to be used in EXAFS experiments. The EXAFS technique requires a high photon flux and a spectral range of approximately 1000 eV. In the IVU design, the taper mode is typically used to expand the bandwidth of the undulator source for EXAFS detection [33]. In the taper mode, the two out-vacuum girders are tilted. In BL16U1, with a maximum gap taper adjustment range of 0.5 mm, indicating a reproducible mechanical gap difference between the exit and entrance gaps (±0.5 mm [34]), an EXAFS above 5 keV can be obtained. In SSRF, "Taper mode" is also used by the BL15U beamline [5]. However, the taper mode widens the spectrum at the expense of reducing the brilliance of the undulator [33]. We now use the taper mode at the non-focusing end-station for EXAFS detection and the planar mode (taper =0) at the microprobe and sub-microprobe end-stations for focusing. The gap-scan mode, in which the gaps of IVU are adjusted according to energy, will be used in the future.

## 2.2 Beamline optics

The primary optical layout of the beamline is shown in Fig. 1. A toroidal mirror, liquid nitrogen-cooled double-crystal monochromator, high-harmonic rejection mirror, and two pairs of Kirkpatrick–Baez (KB) mirrors were installed on the beamline. The details of all beamline mirrors are listed in Table 2. The layout of the beamline is similar to that of the hard X-ray microfocusing beamline (BL15U1) at the SSRF [5] and the microfocus spectroscopy beamline (I18) at Diamond [24]. A horizontally deflecting toroidal mirror (FMB Oxford), achieved by mechanically bending a sagittal cylindrical mirror, was placed 35 m from the source. A set of water-cooled slits (Slit1, Fig. 1), placed 26 m from the source, were used to define the incoming beam on the toroidal mirror.

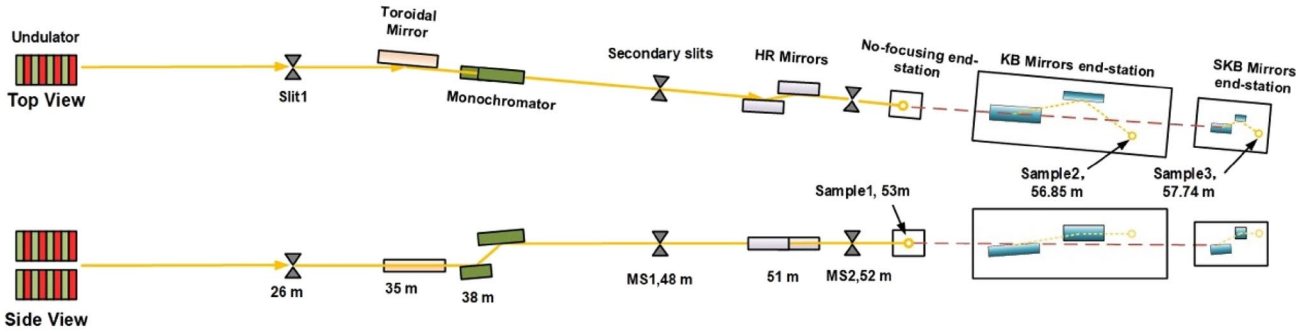


**Fig. 1** (Color online) Schematic showing the principal elements of the beamline

**Table 2** Main specifications of the BL16U1 beamline Mirrors

| | Toroidal Mirror | Harmonic rejection Mirror | KB Mirror | SKB Mirror |
|---|---|---|---|---|
| Type | Cylinder with bender | Flat | (Fixed surface) shape<br>Parabolic for VFM<br>Elliptical for HFM | (Fixed surface shape)<br>Parabolic for VFM<br>Elliptical for HFM |
| Size | 800 mm length<br>25 mm wide | 280 mm length<br>25 mm wide | 22 mm wide<br>300 mm length for VFM<br>340 mm length for HFM | 18 mm wide<br>70 mm length for VFM<br>40 mm length for HFM |
| Mirror material | Silicon | Silicon | Silicon | Silicon |
| Optical quality | Sagittal radius 0.245 m<br>Meridional radius 5.417 km<br>0.3 nm roughness | Sagittal slope error 10 µrad<br>0.3 nm roughness | Sagittal slope error 10 µrad<br>0.3 nm roughness | Sagittal slope error 5 µrad<br>0.3 nm roughness |
| Grazing angle | 3.5 mrad | Cr, 2.05 keV to 3.5 keV, 10 mrad<br>Si, 3.5 keV to 7.5 keV, 3.5 mrad<br>Rh, 7.5 keV to 13 keV, 3.5 mrad | 4 mrad for VFM<br>4.7 mrad for HFM | 4 mrad for VFM<br>4.7 mrad for HFM |
| Coatings | Rh with 10 mm wide<br>Si with 10 mm wide | Cr with 5 mm wide<br>Si with 5 mm wide<br>Rh with 5 mm wide | Ni with 6 mm wide<br>Si with 6 mm wide<br>Rh with 6 mm wide | Ni with 5 mm wide<br>Si with 5 mm wide<br>Rh with 5 mm wide |
| Coatings translation | in vacuum | in vacuum | in vacuum | in vacuum |
| Distance from source | 35 m | 51 m | 56.85 m (focal spot) | 57.74 m (focal spot) |
| Manufacturer | FMB Oxford | TOYAMA | JTEC | JTEC |

Considering the effective length, reflectivity, and heat load, the toroidal mirror was water-cooled and operated at a grazing incidence angle of 3.5 mrad with an active area of 800 mm . The Rh coating on a single-crystal Si substrate was designed for high energies above 8 keV, and the Si coating was designed for photon energies below 8 keV. The two coatings could be switched using an in-vacuum translation mechanism. Typically, to simplify the beamline adjustment, only the Rh coating is used for the entire energy range from 2.1 keV to 16 keV. Using a toroidal mirror, the beam in the vertical plane is collimated, and the influence of vertical source divergence is removed. Thus, energy resolution is primarily a function of the bandpass of the crystals used in the monochromator. In the horizontal plane, the beam was focused onto a secondary source using a mechanical elliptical bend. The secondary slit (MS1 in Fig. 1), placed 48 m away from the light source, was served as the secondary source. The secondary source was used for the horizontal focusing optics of the KB mirrors after the monochromator.

Owing to the high power density of the undulator, a monochromator was installed after the toroidal mirror. A fixed-exit double-crystal monochromator (DCM, TOYAMA) was placed approximately 38 m away from the light source. Photon energies between 2.1 keV to 16 keV with resolution below $1.64 \times 10^{-4}$ ($\Delta E/E$ @ 2.5keV) can be obtained with Si (111) crystal sets. Another set of Si(220) crystal was also applied for better energy resolution, with photon energies ranging from 3.35 keV to 16 keV. The crystals were translated using an in-vacuum translation mechanism. Owing to the high power density of the undulator source, the first and second crystals were indirectly cooled using liquid nitrogen because of the high power density of the undulator source. The fixed-beam exit was maintained by vertically translating the second crystal. The final height difference was selected to be 25 mm. To cover the required energy range, the monochromator has a high-angular range from 0° to 75°. To maintain the alignment of the first and second crystal lattice planes over this angular range, two coarse motors, ±12 mrad and ±8 mrad, were used for roll and pitch coarse adjustment, and two piezo actuators (±0.2 mrad) were used for fine adjustment of the roll and pitch motors.

Two sets of monochromatic four-knife slits without water-cooling were installed downstream of the monochromator. The layout of the beamline slit was similar to that of the microfocus spectroscopy beamline (I18) on Diamond [24]. The first monochromatic four-knife slit (MS1; Fig. 1), 10 m away from the monochromator, serves as the secondary source for focusing optics in the horizontal direction. At this point, the largest slit size is 350 µm × 1400 µm ($h \times v$). Another monochromatic four-knife slit (MS2; Fig. 1), 4 m away from MS1, was used to remove the scatter of the beam at the non-focusing end-station and limit the horizontal and vertical beam sizes onto the KB and smaller KB (SKB) mirrors. At this point, the largest slit size is 1600 µm × 1400 µm ($h \times v$). The slit position was fixed; however, the slit size was controlled using a parallelogram mechanism. The slit size can be changed according to the different spot sizes at the three end-stations.

A harmonic rejection mirror (HRM, TOYAMA) is placed at 51 m from the source. A pair of horizontally reflecting flat silicon mirrors was used to reject higher harmonics. The mirrors had three stripes of chrome (Cr), silicon (Si), and rhodium (Rh), which were vertically translated under vacuum. The Cr reflector can be used for 2.05 keV to 3.5 keV with a grazing incidence angle of 10 mrad. The Si reflector can be used for 3.5 keV to 7.5 keV with a grazing incidence angle of 3.5 mrad. The Rh reflector can be used for 7.5 keV–13 keV with a grazing incidence angle of 3.5 mrad. The grazing incidence angle was regulated by two horizontal vacuum motors installed upstream and downstream of the mirrors. In addition to the three coatings that reflect the X-ray beam, the mirrors can be moved out of the beam in-vacuum translation to ensure that the incoming X-rays pass through without being reflected. In our beamline, owing to the use of Rh coating in the toroidal mirror, the HRM is usually moved out of the beam for energies above 8 keV.

## 3 Experimental station

For XAS and XRF microprobe imaging between 2.1 keV and 16 keV, three end-stations were installed on the BL16U1 beamline, which are the non-focusing end-station, the microprobe, and sub-microprobe end-stations focused by two sets of KB mirrors. A schematic of the layout of the three end-stations is shown in Fig. 2. The specifications of the energy range, energy resolution, flux, and spot size at the different end-stations are listed in Table 3.

The non-focusing end-station is placed approximately 53 m away from the source after the harmonic rejection mirror. X-ray fluorescence (XRF) and X-ray absorption spectroscopy (XAS), including XANES and EXAFS, can be achieved with a spot size of ~ 670 µm × 710 µm. After the non-focusing end-station, two sets of KB systems (Motors from CINEL, Mirrors from JTEC) were chosen as the microprobe and sub-microprobe tools to focus the secondary source on a spot of micron size (Sample 2) and a spot of submicron size (Sample 3) in two different vacuum vessels (Fig. 2). The two vacuum valves (V1 and V2 shown in Fig. 2) were installed downstream of the non-focusing end-station. Valves were used when the He atmosphere was used in the non-focusing end-station. A liquid in situ end-station will be installed in the future by removing the vacuum tube between V1 and V2, and a Be window will be

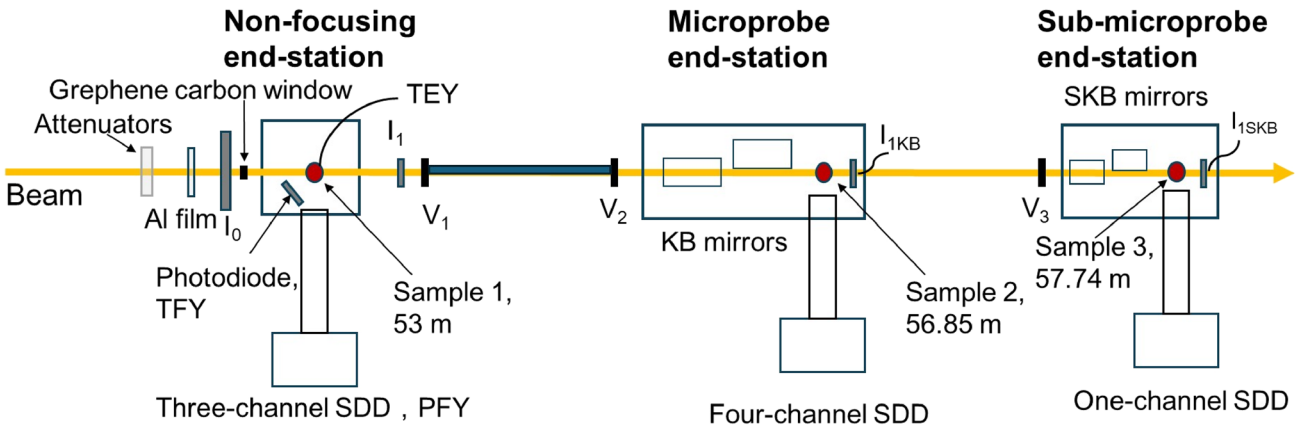


**Fig. 2** (Color online) The schematic layout of the experimental end-stations at BL16U1

**Table 3** Specifications of energy range, energy resolution, flux, and spot size at different end-stations

| End-station | Non-focusing | Micorprobe | Sub-microprobe |
|---|---|---|---|
| Energy range | 2.1 keV to 16 keV | 2.1 keV to 16 keV | 2.1 keV to 16 keV |
| Energy resolution @ 2.5 keV@Si(111) | $1.64 \times 10^{-4}$ | $1.64 \times 10^{-4}$ | $1.64 \times 10^{-4}$ |
| Flux ( photons/s) | $> 2.0 \times 10^{12}$@ 2.15 keV to 13 keV<br>$> 5.0 \times 10^{11}$@ 14 keV to 16 keV | $2.48 \times 10^{12}$@ 10 keV | $7 \times 10^{10}$@ 2.5 keV |
| Spot size (FWHM, $h \times v$) | ~ 670 μm × 710 μm | ~ 3 μm × 1.3 μm | ~ 0.5 μm × 0.25 μm |

installed after the V1 valve to maintain the vacuum in the non-focusing vessel.

The photon flux and energy resolution were obtained at the non-focusing end-station. Figure 3a shows the photon flux measured at $I_1$ of the non-focusing end-station. The designed spot size (full width at half maximum, FWHM) is ~ 670 μm × 710 μm. The photon flux at this station exceeds $2.0 \times 10^{12}$ photons/s for energy between 2.15 keV and 13 keV, and ranges from $1.5 \times 10^{12}$ photons/s to $5.0 \times 10^{11}$ photons/s for 14 keV to 16 keV. This configuration does not represent the optimal status of our beamline; rather, long-term usage can yield better fluxes. Figure 3b shows the rocking curve of 2.5 keV for a Si (111) single crystal. The DCM energy was set to 2.5 keV, and the crystal was rotated in vacuum around 52.2669°. A photodiode (AXUV300C) measured the diffracted photon flux. The FWHM ($\Delta\theta$) at 2.5 keV was ~ 212 μrad, yielding an energy resolution of ~ $1.64 \times 10^{-4}$ by $\Delta\theta / \tan\theta$ (where $\theta$ is 52.2669°).

Micro-XRF (μXRF), micro-X-ray fluorescence mapping, and micro-XANES (μXANES) will be obtained at the KB and SKB microprobe end-stations in the near future. The details of the KB and SKB mirrors are listed in Table 2. Fixed-surface KB mirrors were used for each set. The mirrors substrate were made of Si and coated with Ni, Si, and Rh stripes. The coated stripes were translated using an in-vacuum translation mechanism. A vertical focusing mirror (VFM) and horizontal focusing mirror (HFM) were aligned behind each other in orthogonal planes. The incident angles are 4 mrad and 4.7 mrad for VFM and HFM, respectively.

### 3.1 Non-focusing end-station

The non-focusing end-station is housed in a vacuum vessel, enabling operation in vacuum (1 mbar to $1 \times 10^{-6}$ mbar) or He atmosphere. No load-lock system was used for sample replacement in the non-focusing end-station. Usually, only the dry pump is turned on, and a vacuum of 1 mbar is sufficient for this non-focusing end-station. He gas was purged into the vessel when water was present in the samples, and no vacuum was used. The dry pump and turbo pump (Pfeiffer, HiPace 700) were turned on when high-vacuum and KB systems were used. 20 min to 30 min are need for vacuum vent and samples replacement.

Figure 4 shows a photograph of the non-focusing end-station. A set of translation (*X*-*Z*) and rotation (R) motors (VACGEN) were used to adjust the sample position in the vacuum vessel. The sample holder was ~ 9 cm in total length, with a YAG crystal on top to assist with the beam location (inset in Fig. 4). Samples are usually smeared onto

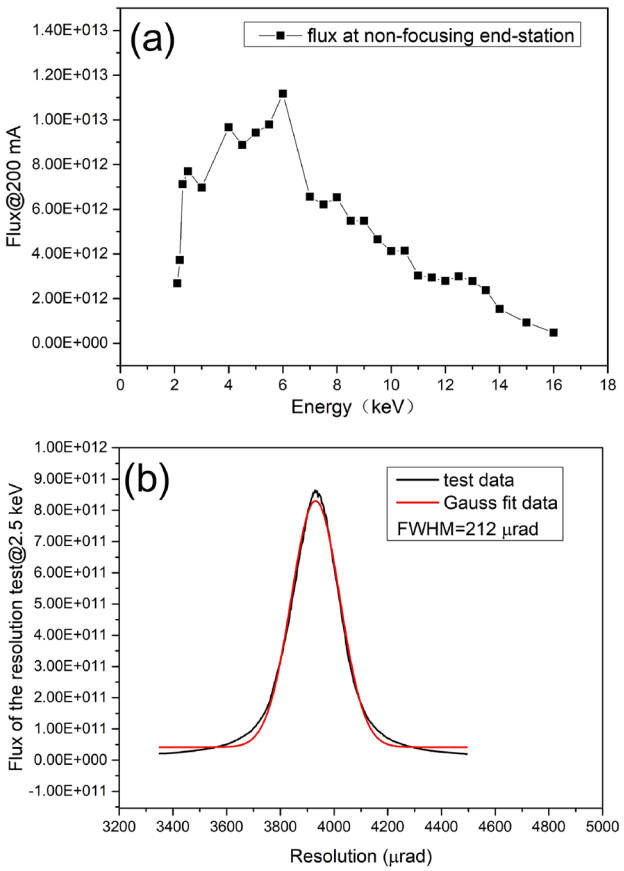


**Fig. 3** (Color online) Flux and rocking curve obtained at the non-focusing end-station. **a** Flux obtained at the non-focusing end-station at 200 mA. **b** Rocking curve obtained after the non-focusing end-station at 200 mA and 2.5 keV

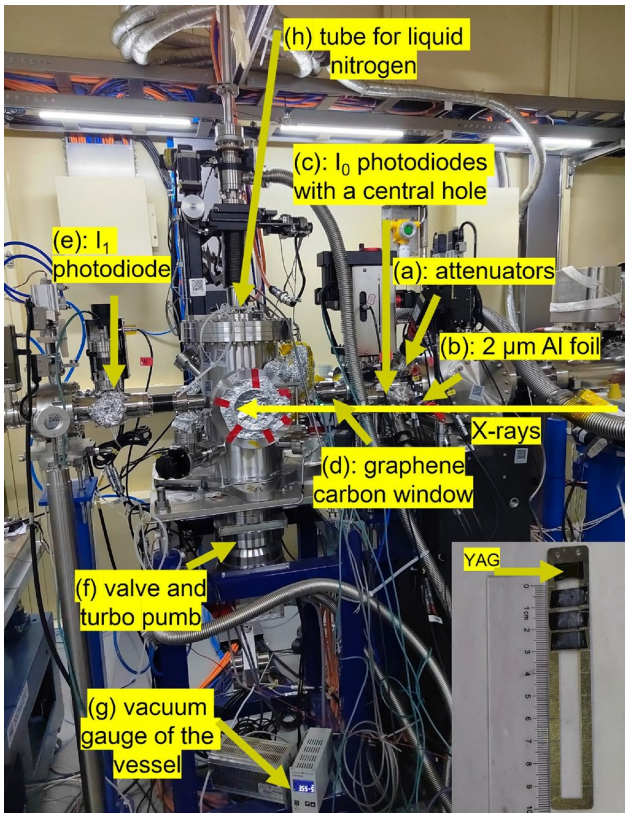


**Fig. 4** (Color online) Photograph of the non-focusing end-station. **a** attenuators used by several Al foils with thickness from 25 μm to 500 μm, **b** Al foil for $I_0$ with thickness of 2 μm, **c** the $I_0$ detector by four photodiodes with a 5 mm pinhole, **d** graphene carbon window, **e** the $I_1$ detector, a normal photodiode, **f** valve and turbo pump for the vessel, **g** vacuum gauge of the vessel, **h** the tube for liquid nitrogen

carbon or Kapton tapes or pressed into disks. Usually, 6–9 samples can be placed on a sample holder simultaneously. By indirectly cooling with liquid nitrogen, the sample in the non-focusing end-station can be operated in vacuum under cryogenic conditions to ~ 120 K. A graphene carbon window (KETEK, ~ 900 nm in thickness and ~ 10 mm in diameter) separated the vacuum of the non-focusing vessel from the beamline. Four photodiodes (AXUV300C) were installed at the four corners of a 5 mm hole to measure the fluorescence after a thin Al film with 2 μm thickness, which was used as the incident beam intensity ($I_0$). Owing to the tight space of the beamline, the $I_0$ detector was placed before the graphene carbon window. Before the $I_0$ detector, several Al foils with different thicknesses (25 μm to 500 μm) were used as attenuators. After samples, a photodiode (AXUV300C) was mounted in the same vacuum vessel to measure the transmitted beam intensity ($I_1$). The $I_1$ photodiode can be removed from the beamline by vacuum translation when a KB microprobe end-station is used. A three-channel silicon drift diode (SDD, RaySpec) with a collimated active area of 150 $mm^2$ was installed perpendicular to the beamline for XRF and partial fluorescence yield (PFY) detection of the sample. A photodiode was installed next to the SDD to measure the total fluorescence yield (TFY) of the samples. The total electron yield (TEY) mode was used to measure the sample current. Schematics of these three detection modes are shown in Fig. 2.

Several XAS results obtained at the non-focusing end-station are shown in Fig. 5. Different XAS detection modes were used based on the morphology, conductivity, and absorption edges of the samples. For elements with absorption edges above 5 keV, the TFY, PFY, and transmission modes were used for XAS detection, according to their morphology and concentration. The TEY, TFY, and PFY modes were used for elements with absorption edges below 5 keV. For the PFY mode with low concentration and the transmission mode with high concentration, the samples should be pressed into disks of proper thickness. For the TEY and TFY modes, the samples are usually smeared onto carbon or Kapton tapes. The $I_0$ and $I_1$ photodiodes shown in Fig. 4 were used for the transmission mode. The P K-edge XANES spectrum of $KH_2PO_4$ in the TEY mode is shown in Fig. 5a.

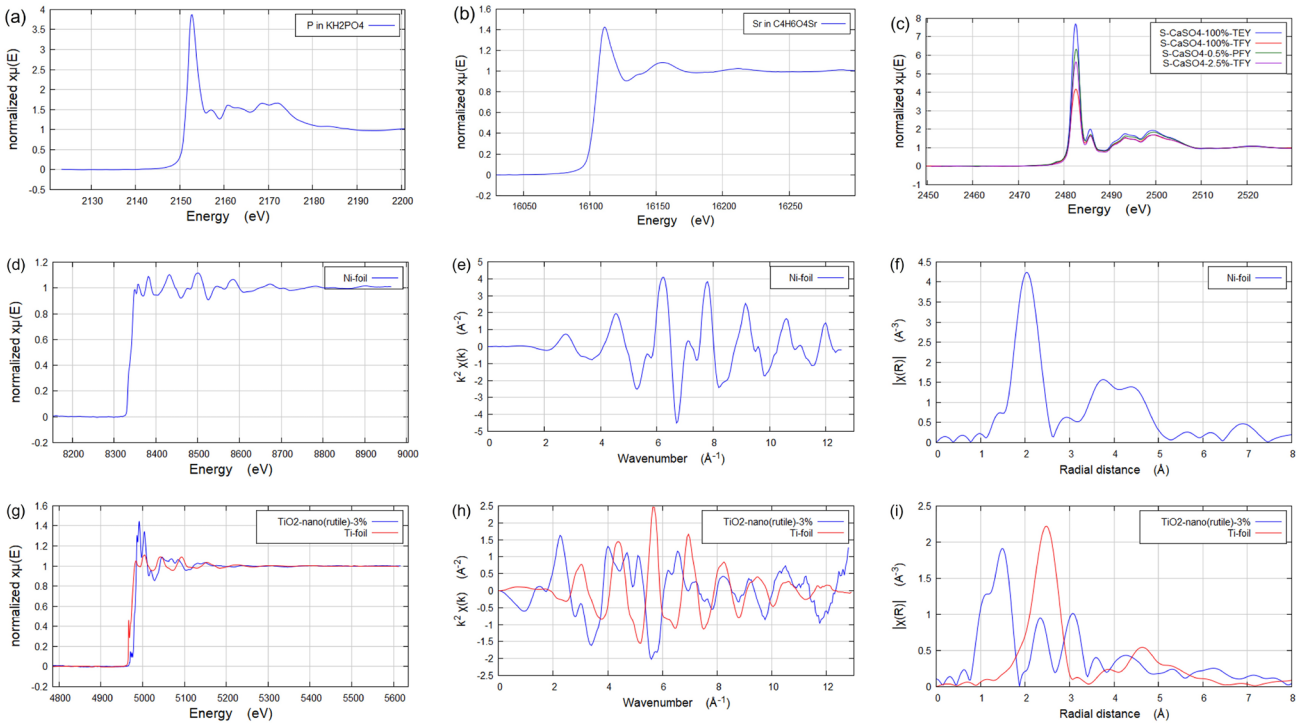


**Fig. 5** (Color online) **a** The normalized P K-edge XANES of $KH_2PO_4$ done by TEY mode, **b** the normalized Sr K-edge XANES of $C_4H_6O_4Sr$ done by transmission mode, **c** the normalized S K-edge XANES of $CaSO_4$ with different concentration done by TFY, TEY and PFY modes, **d** the normalized K-edge XAFS of Ni stand foil done by transmission mode, **e** the EXAFS $k^2\chi$ data and **f** the FT spectra of Ni standard foil, **g** the normalized K-edge XAFS of Ti stand foil done by transmission mode and $TiO_2$-nano (rutile) powder with a mass concentration of 3% done by TFY mode, **h** the EXAFS $k^2\chi$ data and **i** the FT spectra of Ti standard foil and $TiO_2$-nano (rutile) powder

The P K-edge XANES is similar to that of ESRF-ID21 [35]. The max of "white-line" (s→ p electronic transition) of P K-edge of $KH_2PO_4$ is corrected to 2152.8 eV according to ID21 [35]. The Sr K-edge XANES of $C_4H_6O_4Sr$ performed in the transmission mode is shown in Fig. 5b; the spectrum is similar to that of $SrCO_3$ in [36]. The test results showed that the photon energy of the beamline covers the design energy range from 2.1 keV to 16 keV. During the test, each energy integration time was one second with different undulator gaps. The undulator tapper was set to 0.45 mm and the beam current was 220 mA.

The S K-edge XANES spectra of $CaSO_4$ obtained in the TFY, TEY, and PFY modes are shown in Fig. 5c. The S K-edge XANES spectrum is very similar to that of ESRF-ID21 [37]. The max of "white-line" (s→ p electronic transition) of S K-edge of $CaSO_4$ is corrected to 2482.5 eV according to ID21 [37]. High-purity $CaSO_4$ powder and $CaSO_4$ powder diluted with LiF to mass concentrations of 2.5% and 0.5% were used as samples. The $CaSO_4$ powder was smeared evenly onto very thin Kapton or carbon tapes. High-purity $CaSO_4$ powders obtained using the TEY and TFY modes are shown in Fig. 5c. Owing to the self-absorption of fluorescence, the fluorescence spectral signal intensity of TFY (red) was much lower than that of the TEY mode (blue) for samples with high purity. In Fig. 5c, $CaSO_4$ with a 0.5% concentration was performed in the PFY mode (green), and $CaSO_4$ with a 2.5% concentration was performed in the TFY mode (purple). The order of the normalized maximum values was 100% TEY mode, 0.5% PFY mode, 2.5% TFY mode, and 100% TFY mode. Typically, TEY is used for samples with high concentrations, TFY for samples with concentrations between 1% and 5%, and PFY for samples with concentrations of less than 1% [30]. $CaSO_4$ with 0.5% was performed in the TFY mode with a very close working distance between the sample and TFY photodiode (~ 10 mm distance); the spectrum was not very smooth. Thus, the PFY mode was suggested for samples with low concentrations (< 1%).

The K-edge XAFS result of the Ni standard foil (in the transmission mode) is shown in Fig. 5d. The $I_0$ and $I_1$ photodiodes in Fig. 3 were used for the transmission mode. The EXAFS $k^2\chi$ data and Fourier transform (FT) spectra of the Ni standard foil K-edge XAFS spectra are shown in Fig. 5e and f . For energy calibration, the energy and Bragg angle of the DCM were reset according to the first-derivative spectrum of the Ni foil from EXAFS Materials [38]. After energy calibration, the EXAFS $k^2\chi$ data and FT spectra of the Ni standard foil K-edge XAFS spectrum were compared with

those of X18B at the National Synchrotron Light Source [39]. The K-edge XAFS of the Ti standard foil in transmission mode is shown in Fig. 5g. The $I_0$ and $I_1$ photodiodes in Fig. 4 were also used in transmission mode. For comparison, the K-edge XAFS spectrum of $TiO_2$-nano (rutile) diluted with LiF to a mass concentration of 3% was also tested in the TFY mode (Fig. 5g. The energy was also calibrated according to the spectrum of Ti foil from EXAFS Materials. The EXAFS $k^2\chi$ data and FT spectra of the Ti standard foil and $TiO_2$-nano (rutile) are shown in Fig. 5h and i . The EXAFS $k^2\chi$ data and FT spectra of the Ti standard foil K-edge XAFS spectrum can be compared with those of the TPS 44A at the Taiwan Photon Source [40]. The EXAFS and FT spectra of $TiO_2$-nano (rutile) are similar to those obtained in the synchrotron laboratory HASYLAB/DESY, Hamburg [41].

These figures demonstrate that BL16U1 can collect the XAS spectrum across the entire target photon energy range from 2.1 keV to 16 keV. For the tender energy range of 2.1 keV to 5 keV, XANES spectra for phosphorus (P), sulfur (S), chlorine (Cl), potassium (K), and calcium (Ca) are usually collected in the TEY, TFY, and PFY modes. For energies above 5 keV, the XAFS spectra are usually collected in the transmission, TFY, and PFY modes. Although ion chambers are mainly used for synchrotron spectroscopy beamlines worldwide, our results showed that photodiodes can also be used to obtain XANES and XAFS spectra. The only drawback of a photodiode is the diffraction peaks resulting from the crystalline nature of photodiodes [42], which can be removed by the "deglitch" function in the Athena software.

Non-focusing end-station has been in operation for more than one year since the final acceptance test in July 2023. In 2024, this station received more than 85 users with a total user time of 2934 h. Important achievements have been made in many fields, including Co oxidation reactions [43], semi-hydrogenation of propylene [44], and flexible aqueous batteries [45]. This end-station is currently open to the users.

### 3.2 Microprobe and sub-microprobe end-stations

With the aim of analyzing materials at the microscopic scale, microprobe end-stations have been constructed among synchrotron facilities worldwide in recent years (Table 4). A spot size of ~ 2.1 μm × 2.5 μm ($h \times v$) on Daimond I18 [24], a spot size of ~ 2.5 μm × 2.5 μm ($h \times v$) on SLS PHOENIX I [25], a spot size of ~ 0.7 μm × 0.35 μm ($h \times v$), or even smaller than 180 nm on ESRF-ID21 [27], have been achieved using the undulator source. Using a bending magnet source, the spot size in SXRMB beamline at CLS is approximately 10 μm [26] and the spot size in TES beamline at NSLS-II can be tuned from 2 μm to 25 μm [28]. For these microprobe beamlines, KB mirrors are used to focus the beam. Micro-XRF, micro-EXAFS, and micro-X-ray diffraction are the main methods used for these microprobe beamlines.

Here, we focus on the micro-XRF and micro-XANES techniques. Using a multichannel SDD detector, the elemental distribution and correlations of elements can be mapped on a micrometer scale. Using micro-XANES scans, one can obtain the chemical speciation of elements by recording XANES spectra of selected sample spots with grain sizes in the order of micrometers. Micro-XRF and micro-XANES can also be performed on the BL16U1 beamline at the microprobe and sub-microprobe end-stations using two sets of KB mirror systems. The microprobe and sub-microprobe end-stations were installed after the non-focusing end-station. Two sets of KB mirrors were placed in two vacuum vessels, as shown in Fig. 6. The vacuum of the two sets of KB systems was lower than $5 \times 10^{-7}$ mbar using ion pumps, and two sets of load-lock systems were used for sample transfer.

**Table 4** Main specifications of the TES beamline in the world

| Beamline name | Energy range ( keV) | Spot size | Flux ( photons/s) | Research methods |
|---|---|---|---|---|
| Diamond-I18 | 2.05 to 20.7 | 2.1 μm × 2.5 μm | $3.5 \times 10^{12}$@ 8 keV | Micro-XRF, micro-EXAFS micro-XRD |
| SLS-PhoenixI | 0.8 to 8 | 2.5 μm × 2.5 μm | $1 \times 10^{11}$@ 400 mA | Micro imaging and XAFS |
| CLS-SXRMB | 1.7 to 10 | 1 mm × 4 mm<br>10 μm × 10 μm | $10^9$–$10^{11}$@ 100 mA | XAS, XPS, XEOL<br>Micro-XRF and XAFS |
| ESRF-ID21 | 2 to 10 | < 180 nm<br>~ 0.8 μm<br>300 μm to 50 μm | $10^{10}$–$10^{11}$ | Micro and Nano XRF and XANES |
| NSLS-II 8-BM | 2 to 5.5 | 2 μm to 25 μm | Up to $10^{11}$@ 500 mA | Microprobe XRF and EXAFS |
| SPring8 BL27SU | 2.1 to 3.3 | 15 μm × 15 μm | $1 \times 10^{11}$@ 100 mA | Micro-XANES and XRF |
| BSRF 4B7A | 1.75 to 6.0 | 5 mm × 3 mm | $1 \times 10^{11}$@ 2.5 keV | XAS |
| NSRRC TPS 32A | 1.7 to 11 | 0.3 mm × 0.62 mm<br>5 μm × 5 μm | $10^{12}$@ 5 keV | XAS, XAFS, TXPS<br>Micro-XRF and XAFS |

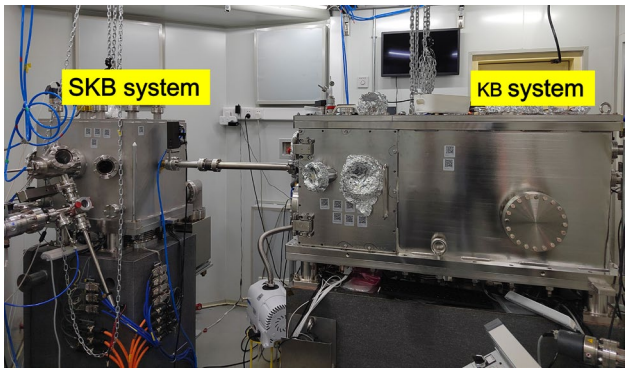


**Fig. 6** (Color online) The vacuum vessels for KB and SKB systems

#### 3.2.1 Microprobe end-station

Using one pair of fixed-surface KB mirrors, the focal spot of the microprobe end-station is approximately 56.85 m from the source. The mirrors substrate were made of silicon and coated with 6 mm wide Ni, Si, and Rh stripes. The coating stripes were translated using an in-vacuum translation mechanism according to energy. A VFM and a HFM were aligned behind each other in orthogonal planes. The incident angles are 4 mrad and 4.7 mrad for VFM and HFM, respectively. Details of the KB mirrors are listed in Table 2.

For the first set of KB mirrors, the focal spot is located at 600 mm and 245 mm from the center of VFM and HFM, respectively, which gives a standard working distance of 75 mm from the end of the HFM to the sample focal plane. A photograph of the KB mirrors and sample stages is shown in Fig. 7a. The mirrors and sample holder were installed in the same vacuum vessel without a vacuum window used for vacuum separation between the KB mirrors and samples. A four-axis sample stage (Micronix) was used for the sample positioning, as shown in Fig. 7b. An angle of 45° exists between the sample's horizontal motion and the beam. The XYZ stages had a scanning precision of 200 nm. A photodiode (AXUV300C) was mounted after the sample holder in the same vacuum vessel to measure the transmitted beam intensity ($I_{1KB}$).

To measure the focal spot size of the KB system, a knife-edge scan using a 50 µm gold wire was used. The knife-edge scan is similar to that performed by Ando et al. [46]. The beam profile was measured using the 50 µm gold wire scanned through the beam, with the intensity of the transmitted beam recorded by a photodiode ($I_{1KB}$) behind the gold wire. The smallest FWHM of the spot size obtained at 10 keV is 4.59 µm × 1.22 µm ($h \times v$), Fig. 7c and d. Because of the 45° angle between the horizontal motion of the sample and beam (Fig. 7b, the horizontal FWHM spot size is obtained by multiplying the Gaussian fitting result with sin 45°; thus, the smallest FWHM of the horizontal spot size at 10 keV is 3.25 µm. Considering the motor resolution, the focal spot size of the KB system should be 3.3 µm × 1.3 µm ($h \times v$). The photon flux at this station was recorded using a photodiode ($I_{1KB}$). The highest current recorded for $I_{1KB}$ was $3.5 \times 10^{-4}$ A @ 10 keV (Fig. 7c and d), the photon flux of the beamline at this station was above $2.48 \times 10^{12}$ photons/s @ 10 keV.

Using the same "$I_0$" mentioned in the non-focusing end-station, µXANES spectra can be done in the KB vessel. A four-channel SDD (Vortex, Hitachi, USA) with a collimated active area of 200 $mm^2$ was installed perpendicular to the beamline for µXRF and PFY detection. Micro-XRF mapping can also be performed in the KB vessel. Because of their windowless design, micro-XRF (µXRF) and micro-XANES (µXANES) can only be achieved under vacuum at the microprobe end-station. Fig. 7e and f shows the µXRF mapping and µXANES spectra of the Cu net. The type of Cu net is GILDER G200-C3. The scan range was 200 µm × 200 µm with a step size of 5 µm.

#### 3.2.2 Sub-microprobe end-station

After the microprobe end-station, a pair of SKB system was employed to focus the beam to a spot size at the submicron level. When the X-ray is focused by the SKB system, the KB mirrors and photodiode in the microprobe end-station should be moved out of the beam by vacuum translation. Similar to the KB system in the microprobe end-station, fixed-surface SKB mirrors with Ni, Si, and Rh stripes were used in the SKB system. The coated stripes were translated using an in-vacuum translation mechanism. Details of the SKB mirrors are provided in Table 2.

For the SKB mirrors, the focal spot is located at 230 mm and 90 mm from the center of VFM and HFM, respectively, which gives a standard working distance of 60 mm from the end of HFM to the sample focal plane. Design drawings of the SKB mirrors and sample stages are shown in Fig. 8a and b . In contrast to the KB system, the mirrors and sample holder were installed in different vacuum vessels separated by a Be window (8 µm thickness and ~ 9.2 mm diameter). Compared to the KB system, the SKB system had a lower flux and smaller spot size. In situ measurements were performed under various conditions at the station. A four-axis sample stage (Micronix) was used to position the sample. An angle of 45° exists between the sample's horizontal motion and the beam. The XYZ stages had a scanning precision of 50 nm. A photodiode (AXUV300C) was mounted after the sample in the vacuum vessel to measure the transmitted beam intensity ($I_{1SKB}$).

With the same incident angles for VFM and HFM, a spot size of 0.67 µm × 0.21 µm can be obtained at 2.5 keV using the SKB system (Fig. 8c and d). An angle of 45° between

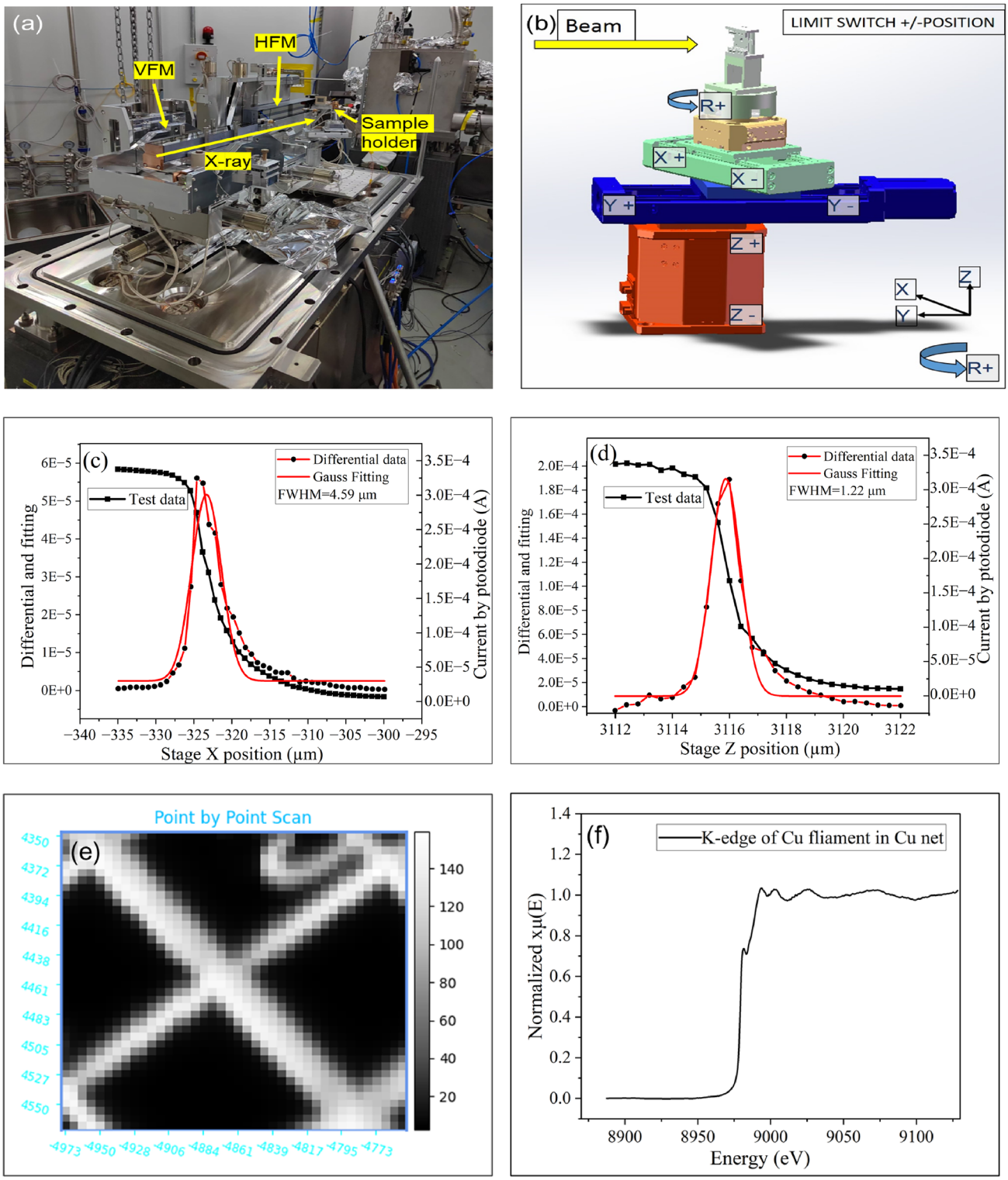


**Fig. 7** (Color online) The photograph of KB mirror system (**a**) and the design view of sample stages (**b**), the horizontal with a 45° angle (**c**), and vertical (**d**) focused beam profiles of KB system at 10 keV. (**e**) The μXRF mapping and (**f**) μXANES of a Cu net

the sample's horizontal motion and the beam was also used in the SKB sample stages (Fig. 8b). The horizontal FWHM spot size is obtained by multiplying the Gaussian fitting result by sin 45°. Thus, the smallest FWHM of the horizontal spot size at 2.5 keV is 0.47 μm. Considering the motor resolution, the focal spot size of the SKB system should be

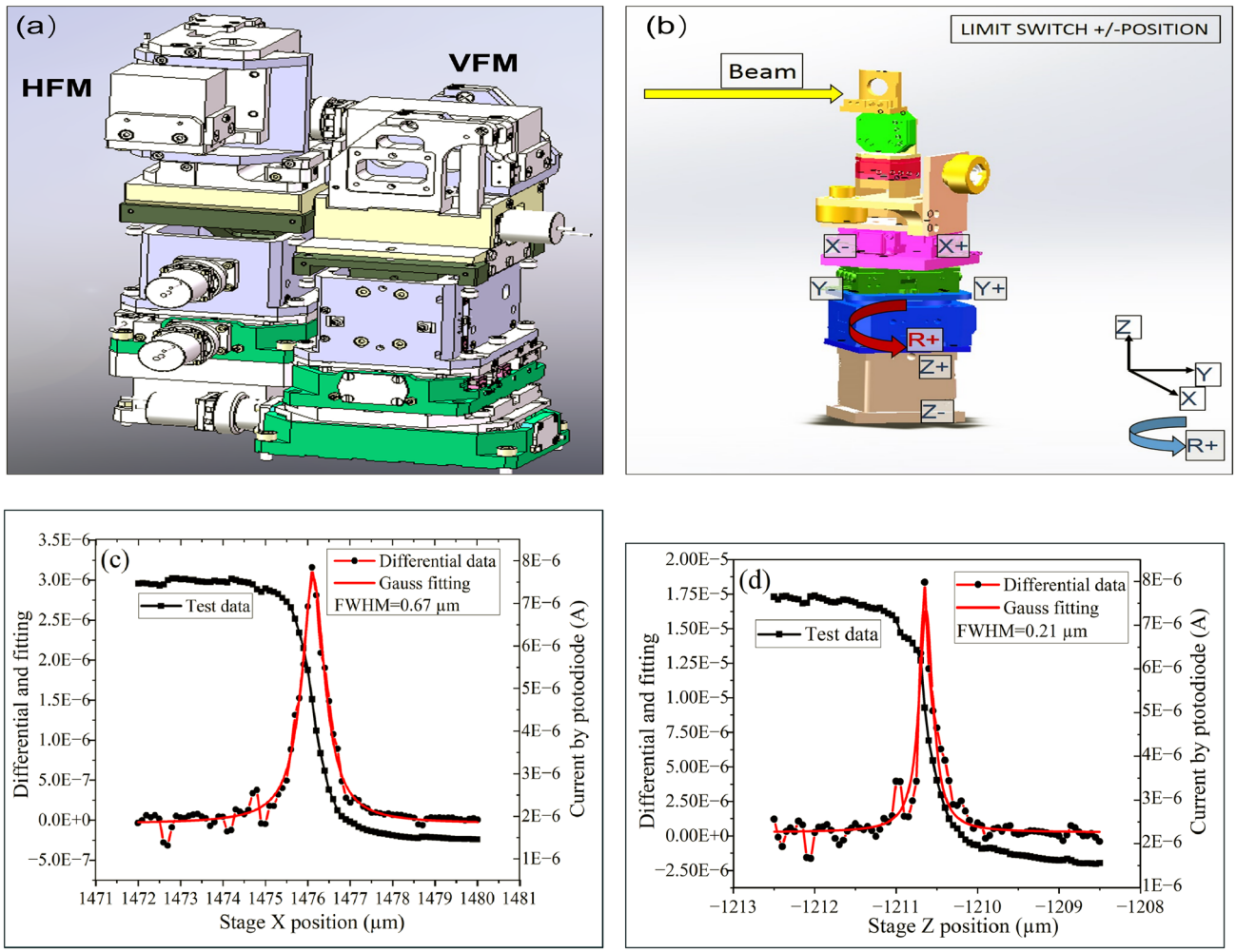


**Fig. 8** (Color online) The design drawing of SKB mirror system (**a**) and the sample stages (**b**), the horizontal with a 45° angle (**c**) and vertical (**d**) focused beam profiles of SKB system at 2.5 keV

$\sim 0.5\,\mu m \times 0.25\,\mu m$ ($h \times v$). The photon flux at this station was recorded using a photodiode ($I_{1SKB}$). The highest current recorded by $I_{1SKB}$ was $7.5 \times 10^{-6}$ A@ 2.5 keV (Fig. 8c and d); the photon flux of the beamline at this station was above $7 \times 10^{10}$ photons/s@ 2.5 keV.

μXAS and μXANES can be performed in the SKB end-station. A one-channel SDD (Vortex, Hitachi, USA) with a collimated active area of 50 $mm^2$ was installed perpendicular to the beamline for μXRF and PFY detection. In contrast to the microprobe end-station, a Be window (8 μm thickness) was used to separate the vacuum of the mirrors and samples. Thus, micro-XRF (μXRF) and micro-XANES (μXANES) under vacuum or He atmosphere can be achieved at the sub-microprobe end-station.

## 4 Summary

The tender energy spectroscopy beamline at SSRF has been completely constructed and opened to users since January 2024. A photon energy between 2.1 keV and 16 keV with resolutions below $1.64 \times 10^{-4}$ ($\Delta E/E$@ 2.5 keV) was obtained at the beamline. XAS spectra performed in transmission, PFY, TEY, and TFY modes were opened to users with a spot size of $\sim 670\,\mu m \times 710\,\mu m$ under vacuum or He atmosphere. Based on two sets of KB mirrors systems, a spot size of approximately $\sim 3.3\,\mu m \times 1.3\,\mu m$ with the photons flux of $2.48 \times 10^{12}$ photons/s@ 10 keV and a smaller spot size of $\sim 0.5\,\mu m \times 0.25\,\mu m$ with the photons flux of $7 \times 10^{10}$ photons/s@ 2.5 kV have been obtained on the microprobe and sub-microprobe end-stations. Micro-XRF (μXRF) and micro-XANES (μXANES) techniques will become available to users in the near future.

**Author Contributions** All authors contributed to the study conception and design. Material preparation, data collection, and analysis were performed by Shu-Min Yang, Ling-Ling Guo, Bing Nan, Ying Zhao, Yan-Qing Wu, Zhi Guo, Chen Tian, Bo Zhao, Chao-Fan Xue, Jun Zhao, Shuang Song, Zhen-Ye Liang, Li-Na Li, Yong Wang, and Ren-Zhong Tai. The first draft of the manuscript was written by Shu-Min Yang, and all authors commented on previous versions of the manuscript. All authors read and approved the final manuscript.

**Data Availability** The data that support the findings of this study are openly available in Science Data Bank at https://cstr.cn/31253.11.sciencedb.j00186.00765 and https://www.doi.org/10.57760/sciencedb.j00186.00765.

## Declarations

**Conflict of interest** Ren-Zhong Tai is an editorial board member for Nuclear Science and Techniques and was not involved in the editorial review, or the decision to publish this article. All authors declare that there are no Conflict of interest.

## References


1. J.H. He, Z.T. Zhao, Shanghai synchrotron radiation facility. Natl. Sci. Rev. **1**, 171–172 (2014). https://doi.org/10.1093/nsr/nwt039
2. M.H. Jiang, X. Yang, H.J. Xu et al., Shanghai synchrotron radiation facility. Chin. Sci. Bull. **54**, 4171–4181 (2009). https://doi.org/10.1007/s11434-009-0689-y
3. R.Z. Tai, Z.T. Zhao, Overview of SSRF phase-II beamlines. Nucl. Sci. Tech. **35**, 137 (2024). https://doi.org/10.1007/s41365-024-01487-1
4. L.X. Yin, R.Z. Tai, D. Wang et al., Progress and future of shanghai synchrotron radiation facility. J. Vac. Soc. Jpn. **59**, 198–204 (2016). https://doi.org/10.3131/jvsj2.59.198
5. L.L. Zhang, S. Yan, S. Jiang et al., Hard X-ray micro-focusing beamline at SSRF. Nucl. Sci. Tech. **26**, 060101 (2015). https://doi.org/10.13538/j.1001-8042/nst.26.060101
6. C. Gu, S. Joshi, M.H.H. Fischel et al., Saltwater intrusion increases phosphorus abundance and alters availability in coastal soils with implications for future sea level rise. Sci. Total Environ. **931**, 172624 (2024). https://doi.org/10.1016/j.scitotenv.2024.172624]
7. D. Hesterberg, I. McNulty, J. Thieme, Speciation of soil phosphorus assessed by XANES spectroscopy at different spatial scales. J. Environ. Qual. **46**, 1190–1197 (2017). https://doi.org/10.2134/jeq2016.11.0431
8. C. Xu, S. Wang, Z. Chen et al., Sulphur speciation and availability in long-term fertilized soil: evidence from chemical fractionation and S K-edge XANES spectroscopy. Eur. J. Soil Sci. **67**, 666–675 (2016). https://doi.org/10.1111/ejss.12364
9. J. Prietzel, A. Botzaki, N. Tyufekchieva et al., Sulfur speciation in soil by S K-edge XANES spectroscopy: comparison of spectral deconvolution and linear combination fitting. Environ. Sci. Technol. **45**(7), 2878–2886 (2011). https://doi.org/10.1021/es102180a
10. A.C. Leri, M.B. Hay, A. Lanzirotti et al., Quantitative determination of absolute organohalogen concentrations in environmental samples by X-ray absorption spectroscopy. Anal. Chem. **78**(16), 5711–5718 (2006). https://doi.org/10.1021/ac060476m
11. L. Monico, L. Cartechini, F. Rosi et al., Synchrotron radiation Ca K edge 2D XANES spectroscopy for studying the stratigraphic Distribution of calcium based consolidants applied to limestone. Sci. Rep. **10**, 14337 (2020). https://doi.org/10.1038/s41598-020-71105-8
12. W. Tan, J.R. Peralta-Videa, J.L. Gardea-Torresdey, Interaction of titanium dioxide nanoparticles with soil components and plants: current knowledge and future research needs - a critical review. Environ. Sci. Nano **5**, 257–278 (2018). https://doi.org/10.1039/C7EN00985B
13. J. Diaz, E. Ingall, C. Benitez-Nelson et al., Marine polyphosphate: A key player in geologic phosphorus sequestration. Scinece **320**, 652–655 (2008). https://doi.org/10.1126/science.1151751
14. J.M. Kleinsasser, B.A. Konecke, A.C. Simon et al., Sulfur speciation in dacitic melts using X-ray absorption near-edge structure spectroscopy of the S K-edge (S-XANES): consideration of radiation-induced changes and the implications for sulfur in natural arc systems. Am. Mineral. **109**(8), 1359–1374 (2024). https://doi.org/10.2138/am-2022-8833
15. A.N. Kravtsova, Synchrotron-based X-ray absorption spectroscopy for the study of geological materials. J. Surf. Investig. **14**, 135–149 (2020). https://doi.org/10.1134/S1027451020020111
16. P. Northrup, A. Leri, R. Tappero, Applications of "Tender'' energy (1–5 keV) X-ray absorption spectroscopy in life science. Protein Pept. Lett. **23**(3), 300–308 (2016). https://doi.org/10.2174/0929866523666160107114505
17. M. Plouviez, B. Guieysse, O. Buwalda et al., Phosphorus storage in microalgae: STXM and XAS P K-edge investigation. ACS Sustainable Resour. Manage. **1**(6), 1270–1278 (2024). https://doi.org/10.1021/acssusresmgt.4c00130
18. M. Gnida, E.Y. Sneeden, J.C. Whitin et al., Sulfur X-ray absorption spectroscopy of living mammalian cells: an enabling tool for sulfur metabolomics. In situ observation of uptake of taurine into MDCK cells. Biochemistry **46**(51), 14735–14741 (2007). https://doi.org/10.1021/bi701979h
19. T. Wang, T.Q. Zhu, Z.Y. Feng et al., Synchrotron radiation-based multi-analytical approach for studying underglaze color: the microstructure of Chinese Qinghua blue decors (Ming dynasty). Anal. Chim. Acta **928**, 20–31 (2016). https://doi.org/10.1016/j.aca.2016.04.053
20. W. Xu, S. Lang, K. Wang et al., Fundamental mechanistic insights into the catalytic reactions of Li-S redox by Co single-atom electrocatalysts via operando methods. Sci. Adv. **9**, eadi5108 (2023). https://doi.org/10.1126/sciadv.adi5108
21. X.J. Zhu, Q.S. Guo, Y.F. Sun et al., Optimising surface d charge of AuPd nanoalloy catalysts for enhanced catalytic activity. Nat. Commun. **10**(1), 1428 (2019). https://doi.org/10.1038/s41467-019-09421-5
22. V.A. Schoepfer, M.B.J. Lindsay, X-ray absorption spectroscopy and X-ray diffraction data for molybdenum minerals and compounds. Data Brief **45**, 108576 (2022). https://doi.org/10.1016/j.dib.2022.108576
23. T.R. Kulp, L.G. Miller, F. Braiotta et al., Microbiological reduction of Sb(V) in anoxic freshwater sediments. Environ. Sci. Technol. **48**, 218–226 (2014). https://doi.org/10.1021/es403312j
24. J. Frederick, W. Mosselmans, P.D. Quinn et al., I18 the microfocus spectroscopy beamline at the Diamond Light Source. J. Synchrotron Rad. **16**, 818–824 (2009). https://doi.org/10.1107/S0909049509032282
25. M.A. Brown, A.B. Redondo, I. Jordan et al., A new endstation at the Swiss Light Source for ultraviolet photoelectron spectroscopy, X-ray photoelectron spectroscopy, and X-ray absorption spectroscopy measurements of liquid solutions. Rev. Sci. Instrum. **84**, 073904 (2013). https://doi.org/10.1063/1.4812786
26. Q. Xiao, A. Maclennan, Y. Hu et al., Medium-energy microprobe station at the SXRMB of the CLS. J. Synchrotron Rad. **24**, 333–337 (2017). https://doi.org/10.1107/S1600577516017604

27. M. Cotte, E. Pouyet, M. Salomé et al., The ID21 X-ray and infrared microscopy beamline at the ESRF: status and recent applications to artistic materials. J. Anal. At. Spectrom. **32**, 477–493 (2017). https://doi.org/10.1039/c6ja00356g
28. P. Northrup, The TES beamline (8-BM) at NSLS-II: tender-energy spatially resolved X-ray absorption spectroscopy and X-ray fluorescence imaging. J. Synchrotron Rad. **26**, 2064–2074 (2019). https://doi.org/10.1107/S1600577519012761
29. H. Ohashi, E. Ishiguro, Y. Tamenori et al., Outline of soft X-ray photochemistry beamline BL27SU of SPring-8. Nucl. Instrum. Methods Phys. Res. A **467–468**, 529–532 (2001). https://doi.org/10.1016/S0168-9002(01)00404-1
30. L. Zheng, Y.D. Zhao, K. Tang et al., A new experiment station on beamline 4B7A at Beijing Synchrotron Radiation Facility. Spectrochim. Acta Part B Atom. Spectrosc. **101**, 1–5 (2014). https://doi.org/10.1016/j.sab.2014.07.006
31. D.G. Liu, M.H. Lee, Y.J. Lu et al., Design of tender X-ray absorption spectroscopy beamline in Taiwan Photon Source. J. Phys. Conf. Ser. **2380**, 012041 (2022). https://doi.org/10.1088/1742-6596/2380/1/012041
32. H. Xie, G. Du, K. Li et al., Development of fast X-ray imaging beamline at SSRF. Proc. SPIE **12169**, 121693B (2022). https://doi.org/10.1117/12.2623647
33. N.E. Sung, I.J. Lee, S. Jeong et al., Characteristics of a tapered undulator for the X-ray absorption fine-structure technique at PLS-II. J. Synchrotron Rad. **21**, 1282–1287 (2014). https://doi.org/10.1107/S1600577514015549
34. Z.Q. Jiang, H.W. Du, C. Chen et al., Supporting and driving system for in-vacuum undulator. Nucl. Sci. Tech. **22**, 1–4. (2011) https://doi.org/10.13538/j.1001-8042/nst.22.1-4
35. ID21 phosphorus XANES spectra database. https://www.esrf.fr/home/UsersAndScience/Experiments/XNP/ID21/id21-phosphorus-xanes-spectra-database/database-inorganic-phosphorous-compounds.html
36. W.R. Bower, K. Morris, J.F.W. Mosselmans et al., Characterising legacy spent nuclear fuel pond materials using microfocus X-ray absorption spectroscopy. J. Hazard. Mater. **317**, 97–107 (2016). https://doi.org/10.1016/j.jhazmat.2016.05.037
37. ID21 sulfur XANES spectra database home. https://www.esrf.fr/files/live/sites/www/files/UsersAndScience/Experiments/XNP/ID21/php/gypsum/gypsum.pdf
38. Reference X-ray spectra of metal foils. https://www.lsu.edu/camd/files/Reference_X-Ray_Spectra_for_Metal_Foils.pdf
39. S. Khalid, W. Caliebe, P. Siddons et al., Quick extended x-ray absorption fine structure instrument with millisecond time scale, optimized for In Situ applications. Rev. Sci. Instrum. **81**, 015105 (2010). https://doi.org/10.1063/1.3276679
40. C.W. Pao, J.L. Chen, J.F. Lee et al., proposed a new X-ray absorption fine-structure beamline with subsecond time resolution at the Taiwan Photon Source. J. Synchrotron Rad. **28**, 930–938 (2021). https://doi.org/10.1107/S1600577521001740
41. K. Schneider, D. Zajac, M. Sikora et al., XAS study of $TiO_2$-based nanomaterials. Radiat. Phys. Chem. **112**, 195–198 (2015). https://doi.org/10.1016/j.radphyschem.2015.03.010
42. G. Dalba, P. Fornasini, Y. Soldo et al., PIN silicon diodes as EXAFS signal detectors. J. Synchrotron Rad. **3**, 213–219 (1996). https://doi.org/10.1107/S0909049596006073
43. Y. Li, L. Guo, M. Du et al., Unraveling distinct effects between CuOx and PtCu alloy sites in Pt-Cu bimetallic catalysts for CO oxidation at different temperatures. Nat. Commun. **15**, 5598 (2024). https://doi.org/10.1038/s41467-024-49968-6
44. K. Yan, X. Ge, W. Li et al., Regulation of a $Ni_3Sn_2$ intermetallic catalyst using highly dispersed Pd species to boost propyne semihydrogenation. J. Mater. Chem. A **12**, 16482–16490 (2024). https://doi.org/10.1039/d4ta02342k
45. M. Lin, R. Qi, W. Zhang et al., Unravelling ultra-stable conversion-type zinc-ion storage in copper selenides for flexible aqueous batteries. Adv. Energy Mater. **14**, 2401288 (2024). https://doi.org/10.1002/aenm.202401288
46. H. Ando, M. Horio, Y. Takeo et al., Developing a simple scanning probe system for soft X-ray spectroscopy with a nano-focusing mirror. e-J. Surf. Sci. Nanotechnol. **21**, 200–206 (2023). https://doi.org/10.1380/ejssnt.2023-020